Supplement of Atmos. Chem. Phys., 26, 1179–1192, 2026
https://doi.org/10.5194/acp-26-1179-2026-supplement

Atmospheric Chemistry and Physics
Open Access
EGU

Supplement of

Assessment of methane emissions from US onshore oil and gas production using MethaneAIR measurements

Katlyn MacKay et al.

Correspondence to: Katlyn MacKay (kmackay@edf.org) and Ritesh Gautam (rgautam@edf.org)

Table of Contents

S1. MethaneAIR quantification of total regional emissions

The MethaneAIR emissions quantification approach uses a hybrid framework consisting of a discrete point source detection and quantification algorithm, and an inverse model of dispersed area sources to estimate the total regional methane emissions at the time of observation. This framework is made possible by the instrument's ability to produce a detailed map of methane emissions at a snapshot in time with high spatial resolution, wide spatial coverage, and high precision.

For each MethaneAIR flight, discrete point source emissions (with methane emission rates > ~200 kg/hr), are detected using an automated threshold-based method with manual QA/QC prior to their inclusion in our analysis and subsequently quantified using a divergence integral (DI) method (Chulakadabba et al., 2023; Warren et al., 2025). The plume detection method first calculates the flux divergence for 600 m x 600 m squares tiled across the scene, using High-Resolution Rapid Refresh (HRRR) wind fields and the divergence integral method (Chulakadabba et al., 2023) to calculate the flux through each square. In the gridded flux product, hotspots were identified with a thresholding method as potential plume origins. At each flux hotspot, we found XCH_4 clumps with a given number of contiguous pixels above a threshold value to create a mask of the plume. We calculated the major axis of the XCH_4 mask and took the upwind end of the major axis (using the HRRR wind direction) to be the plume origin (Warren et al., 2025). This system has been validated with controlled release experiments (Chulakadabba et al., 2023; El Abbadi et al., 2024), and is explained in greater detail in Chulakadabba et al., 2023 and Warren et al., 2025.

With discrete sources ($s_{discrete}$) fixed, the inverse model fits a gridded field of dispersed area source emission rates ($s_{dispersed}$) to account for the balance of the methane enhancement. A gridded field of emission rates in the domain of interest, ($s_{reported} = s_{discrete} + s_{dispersed}$), and "pseudo-emission" rates in the upwind boundary inflow region (s_{inflow}) are fitted to observed column-averaged dry-air mole fractions of methane (XCH_4), z, linked by a Jacobian (H) plus a field of background concentrations (b) (Equation S1).

$$z = H(s_{discrete} + s_{dispersed} + s_{inflow}) + b \quad \text{(Eq. S1)}$$

The inversion enforces non-negative fluxes and exact conservation of the observed methane mass to maintain physical realism and applies Tikhonov regularization to promote spatial smoothness and mitigate the sensitivity of the hybrid framework to transport errors and measurement noise. We solve for the non-negative emission field ($s = s_{discrete} + s_{dispersed} + s_{inflow}$) that reproduces the MethaneAIR enhancements:

$$J(s) = \|H(s) - (z - b)\|^2 + \lambda^2 \|L(s)\|^2, \quad \text{(Eq. S2)}$$
$$\text{st.} \quad s \geq 0, \quad w^T(H\,s) = M,$$

where:
L – first-order spatial difference operator enforcing smoothness
λ – Tikhonov regularization strength (0.5)
M – total methane mass enhancement in the domain (kg CH_4)
w – air-mass weights converting ppb to methane mass

XCH_4 observations were aggregated to 0.01° x 0.01° while preserving their location in time (allowing for overlapping observations from successive flight tracks). Aggregated grid cells at least 50% covered with data that passed all QA/QC flags were included in the analysis.

The Jacobian was computed using the Stochastic Time-Inverted Lagrangian Transport (STILT) model (Fasoli et al., 2018; Lin et al., 2003), which simulates the sensitivity of XCH_4 observations to sources on the ground by propagating air parcel trajectories backwards in time. The Jacobian was computed on a 0.01° x 0.01° grid over a 10° x 10° domain around the center of the flight with trajectories long enough to fully exit the domain or include the previous day's boundary layer (28 hours backtime). Where possible, the Jacobian was computed twice, 1) with STILT driven by meteorological data from the operational Global Forecast System (GFS) model and 2) with STILT driven by meteorology from the High-Resolution Rapid Refresh (HRRR) model. Meteorological data was provided by the NOAA ARL meteorological archives in ARL format (https://www.ready.noaa.gov/archives.php). STILT was run as a column receptor, with a receptor placed at every layer of the meteorological input from the surface to 3x the

planetary boundary layer height (above which we assume the footprint is always 0). STILT footprints for every layer are integrated with weights representing the fraction of the total atmospheric column of dry air represented, with the mean averaging kernel for MethaneAIR.

The background concentration field represents the synoptic-scale, topographically varying component of the XCH_4 observations. We fit a field of background XCH_4 concentrations given by the MethaneAIR L2 prior (Chan Miller et al., 2024) from below, such that the reflected distribution of concentrations below background have a variance that matches the instrument precision. The MethaneAIR L2 prior forms a surface that varies realistically with topography in accordance with the vertical distribution of methane in the atmosphere from GEOS-FP Reanalysis (Rienecker et al., 2008) and the high-resolution digital elevation map tiles from Amazon Web Services (Larrick et al., 2020). Emissions are reported in a truncated domain of interest within the concave hull of the observations.

Boundary inflow "pseudo-emissions" are the component of the dispersed area source emissions inside the full 10° x 10° domain but outside the domain of interest. We refer to them as "pseudo-emissions" since they represent any source of sub-synoptic scale variation in the inflowing methane field, whether from mesoscale background variation or inflow of sources just outside the domain of interest.

Discrete sources are fixed in the area source inversion, fixing emissions in a 0.01° x 0.01° area, which approximates the effective representative area of the DI. This places trust in the well-tested point-source specific algorithm to do the best job at quantifying point source emissions and uses the Jacobian to ensure the complete mass of methane from the point sources are accounted for. The alternative method of plume-masking is inconsistent between methodologies and inevitably undercounts the contribution of the point sources when they fall below detectable concentrations. We acknowledge that this approach may attribute some fraction of discrete-source plume tails to the diffuse component, but this does not affect the basin-integrated emission total, which is constrained by the hard mass constraint. The same observations can influence both the discrete-source estimates and the dispersed-source solution, without explicit propagation of uncertainty from the discrete-source step into the dispersed inversion. A fully Bayesian treatment would require either (i) joint inference of discrete and dispersed emissions within a single probabilistic framework, or (ii) propagation of uncertainty from the discrete-source estimates into the dispersed inversion. Because neither is done here, interpreting the dispersed solution as a Bayesian posterior would be incomplete. Therefore, we deliberately adopt a non-Bayesian framing and report only the deterministic optimal solution of the constrained optimization, rather than probabilistic confidence intervals or posterior distributions.

The inverse problem is then solved numerically using projected, limited memory, bounded Broyden-Fletcher-Goldfarb-Shanno (L-BFGS-B) algorithm. The solution is initialized to a flat field that satisfies the mass constraint. Subsequent proposals are constrained to be non-negative and satisfy the mass constraint. The two constraints regularize the solution to prevent overfitting. The non-negativity constraint mediates the "dipole effect" where adjacent large positive and negative emissions are generated by the inverse model to fit variations in concentrations that cannot be explained by positive emissions alone (e.g., large plumes in areas where the meteorological product has wind direction errors, or variations due to eddies that cannot be modeled by STILT). The mass-balance constraint prevents the emergence of bias when there are high frequency variations that cannot be fit by the model, which may lead the model to over-predict the total emissions. The non-negativity and mass-balance constraint are complementary to the Tikhonov term such that non-negativity enforces physical feasibility, the hard mass constraint enforces domain-scale consistency, and λ controls spatial roughness and suppresses fitting of retrieval/transport noise at small scales. A value of λ=0.5 was selected using an L-curve criterion computed over a set of representative scenes.

The resulting analysis of MethaneAIR data produces a high resolution, spatially explicit quantification of methane emissions at approximately 1 km by 1 km resolution, as well as the specific location and quantification of individual point sources emitting above ~200 kg/hr.

Uncertainty in the MethaneAIR total area emissions estimation is contributed by several factors including (i) uncertainty in the meteorological product used to generate the STILT Jacobian that links emissions with concentrations, (ii) correlated uncertainty in the observations, (iii) uncertainty in the background concentration, (iv) uncertainty in the allocation of signal between emissions in the reported domain and the boundary inflow, and (v) uncertainty in the retrieval of emissions as expressed by the variability in samples in the Markov Chain Monte Carlo

(MCMC) simulation. We use a bootstrap resampling of the MCMC samples to estimate uncertainty, with propagation of uncertainty from each of the above effects by either sweeping across values of input parameters (for example, recomputing the optimization with high and low estimates of the mean background concentration) or modifying each sample (for example, error in the wind speed may increase or decrease all emissions by ±20%). Uncertainty at each grid-level emissions is the 95% confidence interval of samples for that pixel. Uncertainty on the total area emissions is the 95% confidence interval on the total across all samples. The uncertainty estimates for majority of MethaneAIR's individual flight-level observation domains range from ±30% to ±45%, as indicated in Table S4.

S2. Estimating the relative sector contributions of methane emissions quantified by MethaneAIR

S2.1 Data sources used to estimate non-oil and gas methane emissions for each MethaneAIR domain

Table S1 below lists all the publicly available measurement-based and bottom-up data used to estimate the relative contributions of non-oil and gas methane emissions in regions measured by MethaneAIR. The year in brackets next to each referenced study corresponds to the year that the reported emissions estimates are for.

Table S1: Data sources used to estimate contributions of non-oil and gas methane emissions for MethaneAIR measured regions in major oil and gas producing basins.

Sub-Basin	Input data [reference year]
Anadarko	Crippa et al. [2022]; Lu et al. [2019]; Maasakkers et al. [2020]; Nesser et al. [2019]
Appalachian (NE)	Barkley et al. [2017]; Crippa et al. [2022]; Maasakkers et al. [2020]
Appalachian (SW)	Crippa et al. [2022]; Maasakkers et al. [2020]
Arkoma Fayetteville	Crippa et al. [2022]; Lu et al. [2019]; Maasakkers et al. [2020]; Nesser et al. [2019]; Schwietzke et al. [2015]
Bakken	Crippa et al. [2022]; Maasakkers et al. [2020]; Peischl et al. [2015]
Barnett	Crippa et al. [2022]; Lu et al. [2019]; Maasakkers et al. [2020]; Nesser et al. [2019]; Peischl et al. [2015]
Denver	Fried and Dickerson, [2021]; Maasakkers et al. [2020]; Peischl et al. [2015]
Eagle Ford	Crippa et al. [2022]; Lu et al. [2019]; Maasakkers et al. [2020]; Nesser et al. [2019]; Peischl et al. [2015]
Greater Green River	Crippa et al. [2022]; Maasakkers et al. [2020]
Haynesville-Bossier	Crippa et al. [2022]; Lu et al. [2019]; Maasakkers et al. [2020]; Nesser et al. [2019]; Peischl et al. [2015]
Permian (Delaware)	Crippa et al. [2022]; Maasakkers et al. [2020]; Nesser et al. [2019]
Permian (Midland)	Crippa et al. [2022]; Lu et al. [2019]; Maasakkers et al. [2020]; Nesser et al. [2019]
Piceance	Crippa et al. [2022]; Lu et al. [2019]; Maasakkers et al. [2020]; Nesser et al. [2019]
Uinta	Crippa et al. [2022]; Maasakkers et al. [2020]

S2.2. Description of additional method for disaggregation of non-oil and gas sources

As an alternative methodology to the simple subtraction of literature-based non-oil and gas estimates and non-oil and gas point sources quantified by MethaneAIR, we also tested a ratio-based approach that leverages prior estimates of spatially explicit oil and gas and non-oil and gas methane emission inventories. For this approach, we utilize the gridded (0.1° x 0.1°) oil and gas emissions inventory provided in Omara et al., 2024 (EI-ME) which is updated with 2023 activity data, coupled with non-oil and gas emissions from a gridded (0.1° x 0.1°) inventory available from the EPA GHGI inventory for 2020 (Maasakkers et al., 2023), and persistence adjusted methane point source detections from Carbon Mapper (Carbon Mapper, 2025). Both the EI-ME and GHGI methane inventories use the location/density/type of infrastructure data to inform the spatial allocation of methane emissions. The EI-ME is a measurement-based inventory whereas the GHGI is a bottom-up inventory based on reported emissions. These inventories differ from observations gathered from satellite-based studies where we can expect the spatial distribution of emissions to vary over time, despite these emissions estimates being based on prior observations in some cases. We include point sources of methane emissions from Carbon Mapper to account for any additional sources of methane emissions that may not be captured within the EI-ME and GHGI inventories, with the

assumption that potential double-counting of methane sources would occur equally between non-oil and gas and oil and gas methane sources.

Using these spatially explicit methane emissions inventories, we calculate the expected methane emissions for individual grid cells from the area emissions estimates provided by MethaneAIR at their native resolution (1 km x 1 km, or 0.01° x 0.01°). The compiled oil and gas and non-oil and gas emissions from both inventories are then used to calculate a ratio of expected oil and gas emissions, which is then multiplied by the estimated grid-level emissions from MethaneAIR to produce spatially explicit area emissions estimates for oil and gas and non-oil and gas sources (Figure S1). As an additional constraint on uncertainty related to this method, we ascribe area emissions as "unknown" if the measured grid-level estimates from MethaneAIR are more than 100-times higher than the combined emissions from both EI-ME and the GHGI.

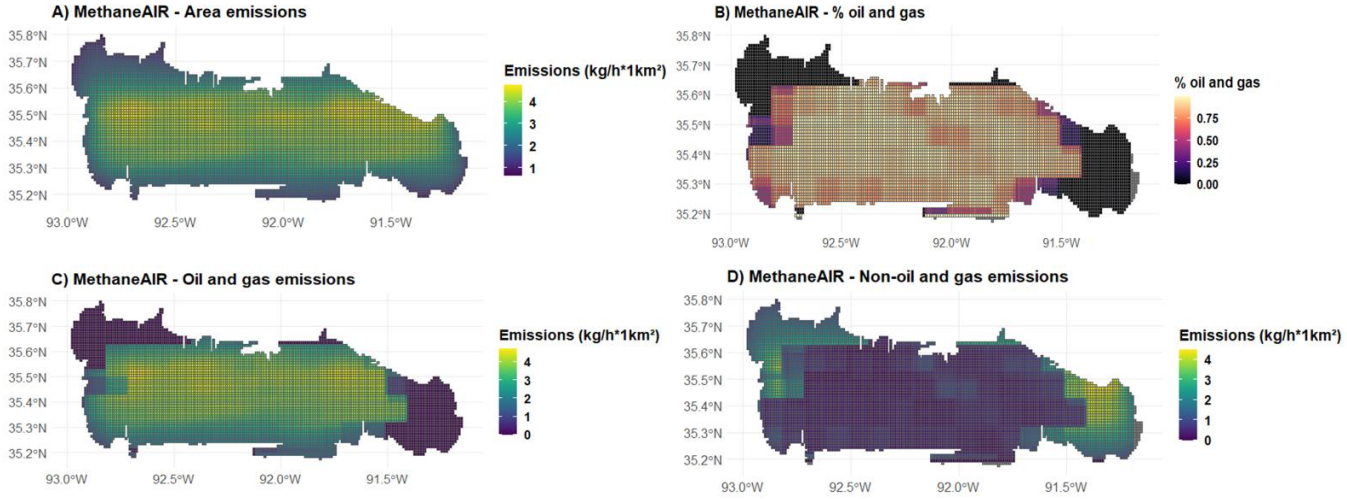

Figure S1: Maps showing disaggregation of oil and gas and non-oil and gas methane emissions from a single MethaneAIR flight in the Arkoma-Fayetteville oil and gas basin as an example. Note that point source emissions are not shown in this figure and are incorporated into total methane emissions using the detailed point source attribution process (Warren et al., 2025). A) Area emissions heatmap from MethaneAIR showing diffuse area source emissions. B) Estimated percentages of oil and gas emissions based on spatially explicit methane emissions data for oil and gas sources (EI-ME: 2023, Omara et al. 2024) and non-oil and gas sources (GHGI inventory: 2020, Maasakkers et al. 2023). C) Heat map of oil and gas emissions from MethaneAIR. D) Heat map of non-oil and gas emissions from MethaneAIR.

S2.3 Comparison of estimated MethaneAIR oil and gas methane emissions across different sector disaggregation methods

We compared total basin-level estimated oil and gas methane emissions using two different methods to disaggregate oil and gas from non-oil and gas area emissions for our MethaneAIR retrievals: the simple subtraction method as presented in the main text, and a ratio-based approach based on a combination of measurement-based and bottom-up estimates (Figure S2). The simple subtraction method estimated an oil and gas total (12 basin sum) of 898 t/hr, whereas the ratio-based method estimated 841 t/hr. We found good agreement (within ~2 t/hr) across both methods in six basins, and moderate agreement (within ~3 – 7 t/hr) in four basins. The biggest discrepancies across methods were in the Greater Green River and Piceance basins, where the ratio-based method produced lower estimates of oil and gas emissions (Figure S2).

In general, the ratio-based method assigns a higher contribution of non-oil and gas emissions due to the spatially widespread presence of agricultural methane emissions whereas other sources of methane emissions (i.e., landfills, oil and gas infrastructure, coal mines) emit at higher amounts per area but are spatially isolated in the prior methane emissions inventories. As such, in areas where MethaneAIR observes dispersed methane emissions without the presence of landfills, oil and gas infrastructure, or coal mines to account for these emissions, they are usually

assigned to agricultural sources, which in turn leads to agricultural emissions that are greater than the total sum contained within the prior estimates. Ultimately, the ratio-based approach incorporates the spatially explicit methane emissions data into the disaggregation process, which provides valuable insights into the presence and location of sector specific methane emissions. In contrast, the simple subtraction method subtracts these values directly from the total methane emissions estimated by MethaneAIR, and therefore the total non-oil and gas emissions match those from the corresponding literature-based estimates from which the value is calculated. While the simple subtraction method does preserve the total non-oil and gas emissions from the literature-based estimates, it does not produce any spatially explicit data on the disaggregated methane emissions.

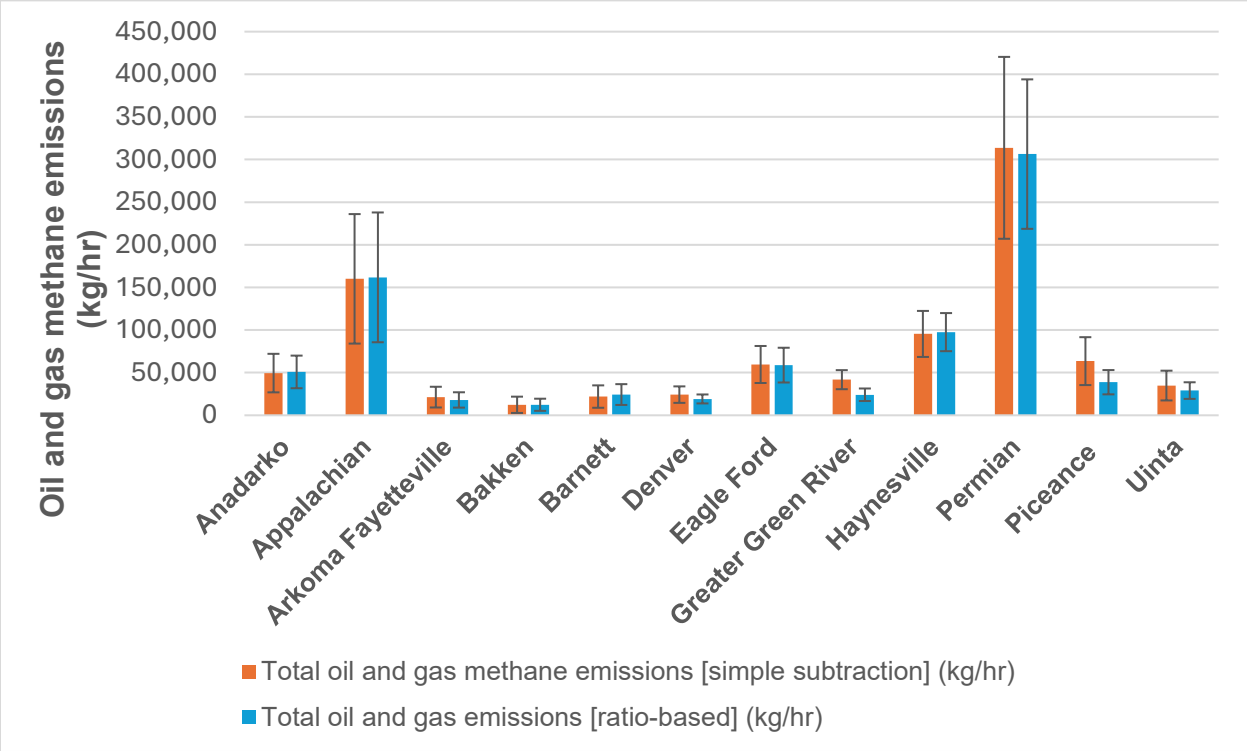

Figure S2: Comparison of estimates of oil and gas emissions for basins measured by MethaneAIR using two different methods: the ratio-based approach, and the simple subtraction method (as presented in the main text).

S3. Methods for basin- and national-level aggregation of MethaneAIR emission estimates – total emissions and associated uncertainties

Two separate approaches for aggregation of overlapping MethaneAIR flights were explored, which we defined as 1) unique overflown area (UOA) averaging, and 2) area-normalized averaging. Results from the UOA averaging method are presented in the main text, and the other method as well as a comparison of results across both approaches are discussed below.

S3.1 Unique overflown area averaging

For the unique overflown area (UOA) averaging method, we start by mapping the spatial domains of each MethaneAIR retrieval to identify areas that were uniquely overflown by the same combination of flights, which creates a subset of smaller spatial domains (Figure S3). Next, we iterated through the subset of smaller spatial domains (i.e., denoted as UOA, or unique overflown areas) and averaged both the point source and area emissions from the corresponding flights. The resulting averages of all UOAs are then summed to produce a total estimate of methane emissions for the aggregated flight domains.

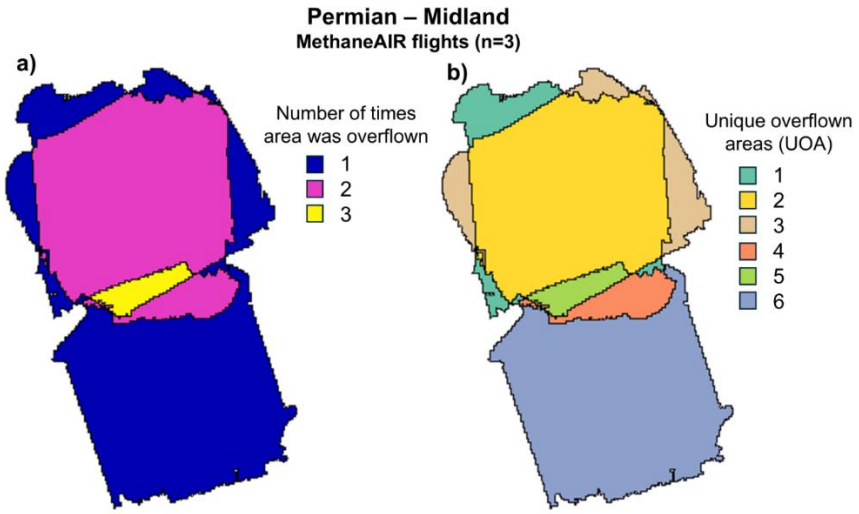

Figure S3: Maps of MethaneAIR flights domains in the Midland portion of the Permian oil and gas basin showing A) the number of times specific areas were overflown by MethaneAIR and B) areas that were overflown by a unique combination of flights (i.e., unique overflown areas or UOA). In this example, six UOAs are created from a combination of three flights in the Midland portion of the Permian basin.

S3.2 Area-normalized averaging approach

For the area-normalized averaging approach, we first normalize the total area and point source methane emissions quantified from each unique flight by the respective area (km^2) covered during the flight to produce an area-normalized flux rate ($kg/hr/km^2$). Then, we compute the total combined area (km^2) covered by all flights for each oil and gas basin. Finally, we calculate the average area normalized flux rates for both area and point source emissions from all flights within a basin and multiply those averages by the total combined area to produce an estimate of the total basin-level emissions.

S3.3 Comparisons of basin-level emissions across different aggregation methods

We compared two different methods used to aggregate multiple MethaneAIR flights to produce basin-level estimates of total methane emissions (Figure S4). Overall, both methods produce similar results across basins, although the differences were larger for the Permian basin with the unique overflown areas method producing 59 t/hr higher estimates compared to the area-averaging method.

The area-normalized method involves dividing total flight-level methane emissions by the total area covered by a given flight, which produces area-normalized methane emission rates. Then, the average area-normalized emissions across all flights are multiplied by the total area covered by the dissolved spatial boundaries of all MethaneAIR flights in a basin which produces a total basin-level emissions estimate. This approach differs from the unique overflow areas approach which weighs emissions by the respective areas covered by individual flights and accounts for areas that have been overflown multiple times. Therefore, we see greater differences in regions where we have multiple flights that have fragmented overlaps with high variability in emission rates by flight (i.e., the Permian basin). Ultimately, the unique overflown areas approach that we use in this work better accounts for the spatial heterogeneity of emissions observed across unique MethaneAIR flights. A more simplistic approach like the area-normalized method is easy to implement but likely carries more uncertainty due to the inherent assumption that the average area-normalized emissions from multiple flights are representative of the entire dissolved spatial domain.

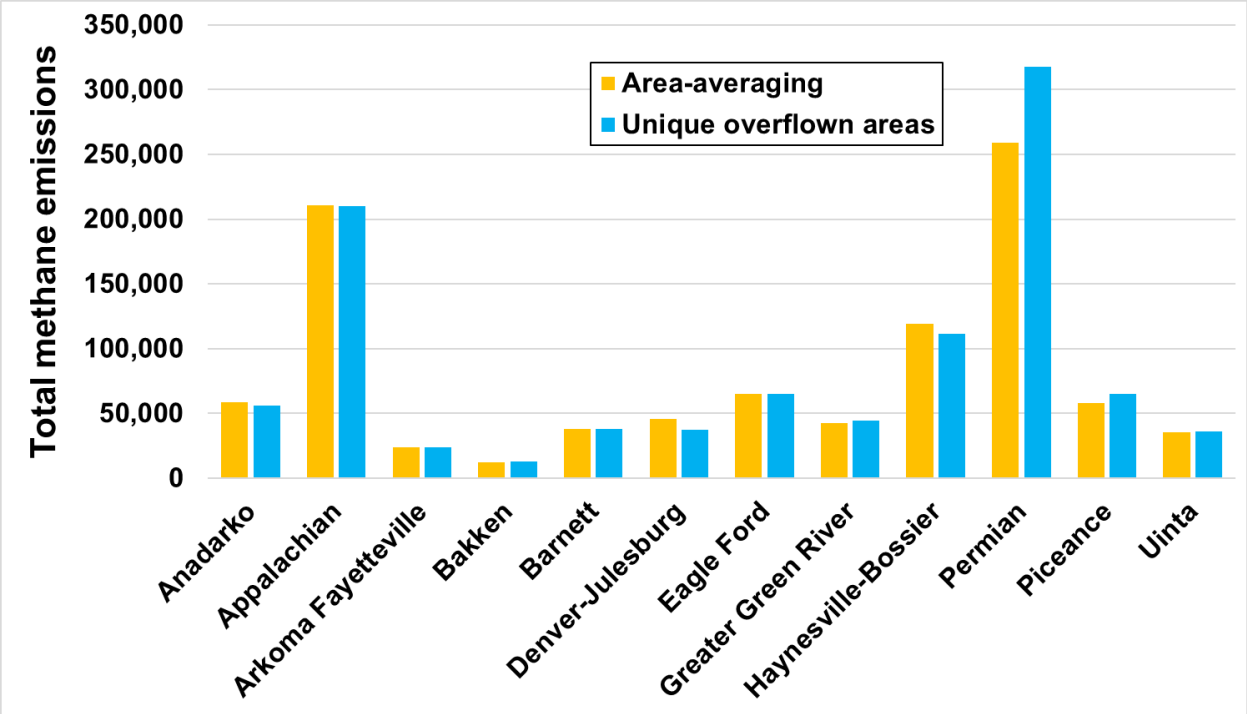

Figure S4: Comparison of the two different methods used to aggregate multiple MethaneAIR flights into basin-level methane emission estimates (kg/hr). Results from the "unique overflown areas" method are presented throughout the main text.

S4. Basin-specific gas compositions used in loss rate calculations

Table S2 shows the basin-specific methane compositions for each basin or sub-basin that were used to calculate the gas-normalized methane loss rates presented in the main text. The methane compositions are applied to the gross natural gas produced in each area measured by MethaneAIR to estimate the gross methane production. The assumed methane compositions are consistent with those reported for each basin in previous literature.

Table S2: Assumed basin specific methane composition of produced gas used in methane loss rate estimates.

Sub-Basin	Assumed methane composition of produced gas
Permian	0.80
Appalachian - NE	0.95
Appalachian - SW	0.90
Anadarko	0.93
Eagle Ford	0.73
Haynesville-Bossier	0.86
Barnett	0.89
Bakken	0.47
San Juan	0.83
Denver-Julesburg	0.79
Uinta	0.89
Arkoma Fayetteville	0.96
Piceance	0.89
Powder River	0.90

Greater Green River	0.92

S5. Energy-normalized methane intensities for measured oil and gas basins

In addition to the gross gas production normalized methane loss rates presented in the main text, we also computed energy-normalized methane intensities (kg CH_4/GJ) for the 12 oil and gas basins measured by MethaneAIR. The main difference between these two metrics is that the energy-normalized methane intensities consider both gross oil and gas produced in each region (Eq. S3), whereas methane loss rates are based on gross gas production only. For energy-normalized methane intensity calculations, gross oil and gas energy production is estimated using 2023 production data (Enverus: Prism, 2024) and a conversion factor of 1 barrel of oil equivalent (boe) = 6 gigajoules (GJ) and 1 boe = 6000 cubic feet of natural gas.

$$Methane\ intensity\ (\frac{kgCH_4}{GJ}) = \frac{Oil\ and\ gas\ methane\ emissions\ (\mathrm{kg})}{(Gross\ natural\ gas\ production\ (\mathrm{GJ}) + Gross\ oil\ production\ (GJ))} \quad \text{(Eq. S3)}$$

Table S3 shows the MethaneAIR gross gas-normalized loss rates (%) and energy-normalized methane intensities (kg CH_4/GJ) for all measured basins. Since methane intensities are based on combined oil and gas production, the basins with the lowest intensities are primarily oil-dominant or mixed basins (e.g., Bakken, Denver-Julesburg), rather than gas-dominant basins (e.g., Appalachian, Haynesville) which have the lowest loss rates. Mature basins with low producing wells rank high across both metrics.

Table S3: Gross gas production normalized methane loss rates (%) and gross energy-normalized (oil + gas) methane intensities (kgCH_4/GJ) estimated for basins measured by MethaneAIR.

Basin	Methane loss rate (%)	Methane intensity (kg CH_4/GJ)
Anadarko	1.4	0.20
Appalachian	0.9	0.15
Arkoma Fayetteville	3.1	0.57
Bakken	2.1	0.06
Barnett	1.6	0.26
Denver-Julesburg	1.3	0.11
Eagle Ford	2.0	0.13
Greater Green River	5.2	0.88
Haynesville-Bossier	0.9	0.15
Permian	2.4	0.15
Piceance	7.9	1.29
Uinta	7.7	0.55

S6. Reported methane emissions for MethaneAIR measured regions based on EPA's 2020 GHGI

Table S4 shows total methane emissions and total oil and gas methane emissions from the EPA GHGI (Maasakkers et al., 2023) for the combined regions measured by MethaneAIR in each basin (as shown in Figure 1 in the main text). Note that these estimates are for the year 2020, which was the most recently available year at the time of writing.

Table S4: EPA 2020 reported total methane emissions and oil and gas methane emissions for MethaneAIR measured regions.

Basin	EPA total methane emissions in MethaneAIR measured regions (kg/hr)	EPA oil and gas methane emissions in MethaneAIR measured regions (kg/hr)

Anadarko	18,200	13,880
Appalachian	49,280	21,630
Arkoma Fayetteville	7,380	5,860
Bakken	5,640	5,210
Barnett	21,700	16,380
Denver-Julesburg	18,200	8,010
Eagle Ford	17,280	14,250
Greater Green River	5,430	5,270
Haynesville-Bossier	31,700	24,760
Permian	52,000	49,030
Piceance	12,300	10,690
Uinta	7,970	7,290

S7. Comparisons of MethaneAIR quantification to literature-based estimates

Table S5 shows total quantified methane emission rates for all MethaneAIR flights included in our analysis, and the corresponding literature-based ranges of total methane emissions for each MethaneAIR flight domain, calculated using bootstrap resampling described in Section 3.3.1.

The MethaneAIR quantification shows generally good agreement with previous literature estimates across all flights, with only four flights (MX031, MX042, MX035, MX037-01) having emission rates that fall more than a factor of two outside the upper/lower bounds. The ranges for MX031, MX035, and MX037-01 are based on limited data which may be why we see the disagreement with the MethaneAIR quantification. During MX042, the largest point source across all flights was detected (69,900 kg/hr), resulting in a total emission rate that is likely higher than what is typical for this region since the point source detection was likely a short-lived emission event. If the point source is removed, the MethaneAIR total emissions for MX042 reduces to 13,500 kg/hr, which is just outside the literature-based range.

Table S5: Total emissions quantified by MethaneAIR for all individual flights included in our analysis and corresponding ranges of total methane emissions for each flight domain based on previous literature estimates.

Basin	Flight ID	MethaneAIR total emissions (kg/hr) and uncertainty	Literature-based range of total methane emissions (kg/hr)	Studies used to develop literature-based ranges
Anadarko	MX059	29,500 (±37%)	18,800 - 38,100	Crippa et al., 2024; Lu et al., 2023; Maasakkers et al., 2023; Nesser et al., 2024; Omara et al., 2024; Shen et al., 2022
Anadarko	MX060	34,400 (±52%)	17,800 - 31,300	Crippa et al., 2024; Lu et al., 2023; Maasakkers et al., 2023; Nesser et al., 2024; Omara et al., 2024; Shen et al., 2022

Appalachian (SW)	MX031	104,500 (±31%)	23,400 - 36,100	Crippa et al., 2024; Cusworth et al., 2022; Maasakkers et al., 2023; Omara et al., 2024
Appalachian (NE)	MX042	83,400 (±54%)	14,400 - 22,100	Alvarez et al., 2018; Barkley et al., 2023, 2017; Crippa et al., 2024; Cusworth et al., 2022; Maasakkers et al., 2023; Omara et al., 2024
Appalachian (SW)	MX045	67,100 (±35%)	36,100 - 65,200	Crippa et al., 2024; Cusworth et al., 2022; Maasakkers et al., 2023; Omara et al., 2024
Arkoma Fayetteville	MX010	23,600 (±37%)	9,300 - 26,500	Alvarez et al., 2018; Crippa et al., 2024; Lu et al., 2023; Maasakkers et al., 2023; Nesser et al., 2024; Omara et al., 2024; Schwietzke et al., 2017
Bakken	MX005	12,500 (±46%)	24,200 - 29,000	Alvarez et al., 2018; Crippa et al., 2024; Maasakkers et al., 2023; Omara et al., 2024; Peischl et al., 2018
Barnett	MX015	38,100 (±41%)	38,400 - 62,300	Alvarez et al., 2018; Crippa et al., 2024; Lu et al., 2023; Maasakkers et al., 2023; Nesser et al., 2024; Omara et al., 2024; Peischl et al., 2018; Shen et al., 2022
Denver-Julesburg	MX013	32,700 (±51%)	23,900 - 30,800	Alvarez et al., 2018; Cusworth et al., 2022; Fried and Dickerson, 2023; Maasakkers et al., 2023; Omara et al., 2024; Peischl et al., 2018; Sherwin et al., 2023
Denver-Julesburg	MX036	28,700 (±32%)	23,700 - 26,600	Alvarez et al., 2018; Cusworth et al., 2022; Fried and Dickerson, 2023; Maasakkers et al.,

				2023; Omara et al., 2024; Peischl et al., 2018; Sherwin et al., 2023
Denver-Julesburg	MX050	31,200 (±34%)	23,900 - 30,100	Alvarez et al., 2018; Cusworth et al., 2022; Fried and Dickerson, 2023; Maasakkers et al., 2023; Omara et al., 2024; Peischl et al., 2018; Sherwin et al., 2023
Denver-Julesburg	MX051	24,500 (±37%)	24,000 - 31,000	Alvarez et al., 2018; Cusworth et al., 2022; Fried and Dickerson, 2023; Maasakkers et al., 2023; Omara et al., 2024; Peischl et al., 2018; Sherwin et al., 2023
Denver-Julesburg	MX061	28,800 (±33%)	23,700 - 29,700	Alvarez et al., 2018; Cusworth et al., 2022; Fried and Dickerson, 2023; Maasakkers et al., 2023; Omara et al., 2024; Peischl et al., 2018; Sherwin et al., 2023
Eagle Ford (N)	MX012	28,400 (±49%)	22,400 - 39,200	Crippa et al., 2024; Lu et al., 2023; Maasakkers et al., 2023; Nesser et al., 2024; Omara et al., 2024; Peischl et al., 2018; Shen et al., 2022
Eagle Ford (S)	MX018	36,400 (±50%)	16,700 - 34,600	Crippa et al., 2024; Lu et al., 2023; Maasakkers et al., 2023; Nesser et al., 2024; Omara et al., 2024; Peischl et al., 2018; Shen et al., 2022
Greater Green River (S)	MX039-South	14,000 (±34%)	3,800 - 7,900	Crippa et al., 2024; Maasakkers et al., 2023; Omara et al., 2024
Greater Green River (E)	MX039-East	28,700 (±33%)	8,300 - 16,900	Crippa et al., 2024; Maasakkers et al., 2023; Omara et al., 2024

Haynesville	MX004	35,200 (±35%)	33,000 - 49,300	Crippa et al., 2024; Lu et al., 2023; Maasakkers et al., 2023; Nesser et al., 2024; Omara et al., 2024; Peischl et al., 2018; Shen et al., 2022
Haynesville	MX016	37,500 (±40%)	32,100 - 51,700	Crippa et al., 2024; Lu et al., 2023; Maasakkers et al., 2023; Nesser et al., 2024; Omara et al., 2024; Peischl et al., 2018; Shen et al., 2022
Haynesville	MX017	88,100 (±35%)	40,000 - 56,900	Crippa et al., 2024; Lu et al., 2023; Maasakkers et al., 2023; Nesser et al., 2024; Omara et al., 2024; Peischl et al., 2018; Shen et al., 2022
Permian (Delaware)	MX023	136,400 (±32%)	53,700 - 76,800	Crippa et al., 2024; Cusworth et al., 2022; Maasakkers et al., 2023; Nesser et al., 2024; Omara et al., 2024; Shen et al., 2022; Varon et al., 2023; Veefkind et al., 2023; Zhang et al., 2020
Permian (Delaware)	MX024	73,200 (±35%)	66,500 - 76,900	Crippa et al., 2024; Cusworth et al., 2022; Maasakkers et al., 2023; Nesser et al., 2024; Omara et al., 2024; Shen et al., 2022; Varon et al., 2023; Veefkind et al., 2023; Zhang et al., 2020
Permian (Delaware)	MX025	40,800 (±35%)	59,600 - 67,200	Crippa et al., 2024; Cusworth et al., 2022; Maasakkers et al., 2023; Nesser et al., 2024; Omara et al., 2024; Shen et al., 2022; Varon et al., 2023; Veefkind et al., 2023; Zhang et al., 2020
Permian (Midland)	MX026	66,600 (±39%)	52,900 - 73,100	Crippa et al., 2024; Cusworth et al.,

				2022; Lu et al., 2023; Maasakkers et al., 2023; Nesser et al., 2024; Omara et al., 2024; Shen et al., 2022; Varon et al., 2023; Veefkind et al., 2023; Zhang et al., 2020
Permian (Midland)	MX027	23,100 (±57%)	39,800 - 50,500	Crippa et al., 2024; Lu et al., 2023; Maasakkers et al., 2023; Nesser et al., 2024; Omara et al., 2024; Shen et al., 2022; Varon et al., 2023; Veefkind et al., 2023; Zhang et al., 2020
Permian (Delaware)	MX056	44,100 (±32%)	46,800 - 60,500	Crippa et al., 2024; Cusworth et al., 2022; Maasakkers et al., 2023; Nesser et al., 2024; Omara et al., 2024; Shen et al., 2022; Varon et al., 2023; Veefkind et al., 2023; Zhang et al., 2020
Permian (Delaware)	MX062	129,100 (±31%)	50,400 - 75,000	Crippa et al., 2024; Cusworth et al., 2022; Maasakkers et al., 2023; Nesser et al., 2024; Omara et al., 2024; Shen et al., 2022; Varon et al., 2023; Veefkind et al., 2023; Zhang et al., 2020
Permian (Midland)	MX063	60,000 (±51%)	46,400 - 64,900	Crippa et al., 2024; Cusworth et al., 2022; Lu et al., 2023; Maasakkers et al., 2023; Nesser et al., 2024; Omara et al., 2024; Shen et al., 2022; Varon et al., 2023; Veefkind et al., 2023; Zhang et al., 2020
Piceance	MX035	49,800 (±31%)	9,300 - 16,600	Crippa et al., 2024; Lu et al., 2023; Maasakkers et al., 2023; Nesser et al., 2024; Omara et al.,

				2024; Shen et al., 2022
Piceance	MX037-01	15,800 (±33%)	3,400 - 5,400	Crippa et al., 2024; Lu et al., 2023; Maasakkers et al., 2023; Nesser et al., 2024; Omara et al., 2024; Shen et al., 2022
Uinta	MX022	31,600 (±33%)	53,700 - 76,800	Crippa et al., 2024; Cusworth et al., 2022; Lin et al., 2021; Maasakkers et al., 2023; Omara et al., 2024; Shen et al., 2022; Sherwin et al., 2023
Uinta	MX037-02	11,700 (±34%)	8,900 - 9,500	Crippa et al., 2024; Maasakkers et al., 2023; Omara et al., 2024; Shen et al., 2022

S8. Observed vs modeled XCH_4 enhancement for all MethaneAIR data used in analysis

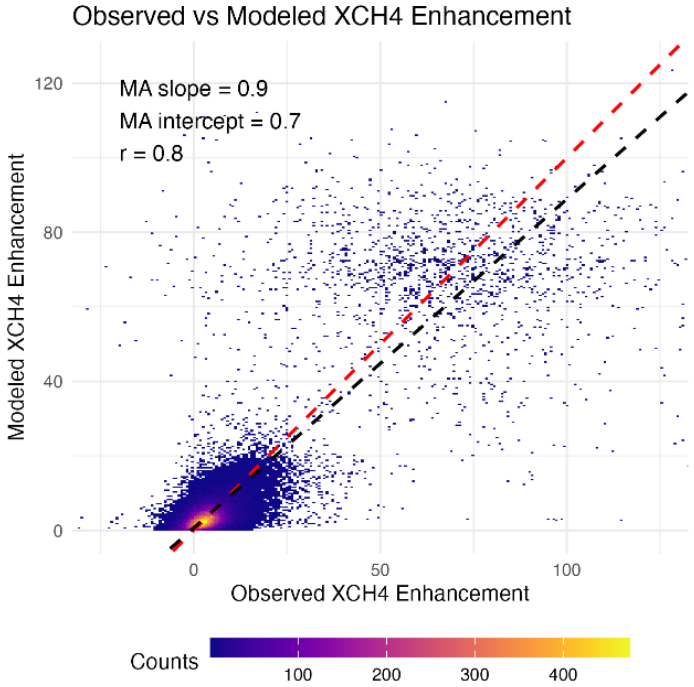

Figure S5: Observed vs modeled XCH_4 enhancement for all MethaneAIR flights. The black dashed line shows the major axis regression, showing a good fit (r = 0.8). The 1:1 relationship is shown as the red dashed line.

References

Alvarez, R. A., Zavala-Araiza, D., Lyon, D. R., Allen, D. T., Barkley, Z. R., Brandt, A. R., Davis, K. J., Herndon, S. C., Jacob, D. J., Karion, A., Kort, E. A., Lamb, B. K., Lauvaux, T., Maasakkers, J. D., Marchese, A. J., Omara, M., Pacala, S. W., Peischl, J., Robinson, A. L., Shepson, P. B., Sweeney, C., Townsend-Small, A., Wofsy, S. C., and

Hamburg, S. P.: Assessment of methane emissions from the U.S. oil and gas supply chain, Science, 361, 186–188, https://doi.org/10.1126/science.aar7204, 2018.

Enverus: Prism: https://www.enverus.com/, last access: 10 October 2024.

Carbon Mapper: https://data.carbonmapper.org/#1.31/30.8/50.5, last access: 24 April 2025.

Barkley, Z., Davis, K., Miles, N., Richardson, S., Deng, A., Hmiel, B., Lyon, D., and Lauvaux, T.: Quantification of oil and gas methane emissions in the Delaware and Marcellus basins using a network of continuous tower-based measurements, Atmospheric Chemistry and Physics, 23, 6127–6144, https://doi.org/10.5194/acp-23-6127-2023, 2023.

Barkley, Z. R., Lauvaux, T., Davis, K. J., Deng, A., Miles, N. L., Richardson, S. J., Cao, Y., Sweeney, C., Karion, A., Smith, M., Kort, E. A., Schwietzke, S., Murphy, T., Cervone, G., Martins, D., and Maasakkers, J. D.: Quantifying methane emissions from natural gas production in north-eastern Pennsylvania, Atmospheric Chemistry and Physics, 17, 13941–13966, https://doi.org/10.5194/acp-17-13941-2017, 2017.

Chan Miller, C., Roche, S., Wilzewski, J. S., Liu, X., Chance, K., Souri, A. H., Conway, E., Luo, B., Samra, J., Hawthorne, J., Sun, K., Staebell, C., Chulakadabba, A., Sargent, M., Benmergui, J. S., Franklin, J. E., Daube, B. C., Li, Y., Laughner, J. L., Baier, B. C., Gautam, R., Omara, M., and Wofsy, S. C.: Methane retrieval from MethaneAIR using the CO_2 proxy approach: a demonstration for the upcoming MethaneSAT mission, Atmospheric Measurement Techniques, 17, 5429–5454, https://doi.org/10.5194/amt-17-5429-2024, 2024.

Chulakadabba, A., Sargent, M., Lauvaux, T., Benmergui, J. S., Franklin, J. E., Chan Miller, C., Wilzewski, J. S., Roche, S., Conway, E., Souri, A. H., Sun, K., Luo, B., Hawthrone, J., Samra, J., Daube, B. C., Liu, X., Chance, K., Li, Y., Gautam, R., Omara, M., Rutherford, J. S., Sherwin, E. D., Brandt, A., and Wofsy, S. C.: Methane point source quantification using MethaneAIR: a new airborne imaging spectrometer, Atmospheric Measurement Techniques, 16, 5771–5785, https://doi.org/10.5194/amt-16-5771-2023, 2023.

Crippa, M., Guizzardi, D., Pagani, F., Schiavina, M., Melchiorri, M., Pisoni, E., Graziosi, F., Muntean, M., Maes, J., Dijkstra, L., Van Damme, M., Clarisse, L., and Coheur, P.: Insights into the spatial distribution of global, national, and subnational greenhouse gas emissions in the Emissions Database for Global Atmospheric Research (EDGAR v8.0), Earth System Science Data, 16, 2811–2830, https://doi.org/10.5194/essd-16-2811-2024, 2024.

Cusworth, D. H., Thorpe, A. K., Ayasse, A. K., Stepp, D., Heckler, J., Asner, G. P., Miller, C. E., Yadav, V., Chapman, J. W., Eastwood, M. L., Green, R. O., Hmiel, B., Lyon, D. R., and Duren, R. M.: Strong methane point sources contribute a disproportionate fraction of total emissions across multiple basins in the United States, Proc. Natl. Acad. Sci. U.S.A., 119, e2202338119, https://doi.org/10.1073/pnas.2202338119, 2022.

El Abbadi, S. H., Chen, Z., Burdeau, P. M., Rutherford, J. S., Chen, Y., Zhang, Z., Sherwin, E. D., and Brandt, A. R.: Technological Maturity of Aircraft-Based Methane Sensing for Greenhouse Gas Mitigation, Environ. Sci. Technol., 58, 9591–9600, https://doi.org/10.1021/acs.est.4c02439, 2024.

Fasoli, B., Lin, J. C., Bowling, D. R., Mitchell, L., and Mendoza, D.: Simulating atmospheric tracer concentrations for spatially distributed receptors: updates to the Stochastic Time-Inverted Lagrangian Transport model's R interface (STILT-R version 2), Geoscientific Model Development, 11, 2813–2824, https://doi.org/10.5194/gmd-11-2813-2018, 2018.

Fried, A. and Dickerson, R.: Continuous Airborne Measurements and Analysis of Oil & Natural Gas Emissions During the 2021 Denver-Julesburg Basin Studies, 2023.

Larrick, G., Tian, Y., Rogers, U., Acosta, H., and Shen, F.: Interactive Visualization of 3D Terrain Data Stored in the Cloud, in: 2020 11th IEEE Annual Ubiquitous Computing, Electronics & Mobile Communication Conference (UEMCON), 2020 11th IEEE Annual Ubiquitous Computing, Electronics & Mobile Communication Conference (UEMCON), 0063–0070, https://doi.org/10.1109/UEMCON51285.2020.9298063, 2020.

Lin, J. C., Gerbig, C., Wofsy, S. C., Andrews, A. E., Daube, B. C., Davis, K. J., and Grainger, C. A.: A near-field tool for simulating the upstream influence of atmospheric observations: The Stochastic Time-Inverted Lagrangian Transport (STILT) model, Journal of Geophysical Research: Atmospheres, 108, https://doi.org/10.1029/2002JD003161, 2003.

Lin, J. C., Bares, R., Fasoli, B., Garcia, M., Crosman, E., and Lyman, S.: Declining methane emissions and steady, high leakage rates observed over multiple years in a western US oil/gas production basin, Sci Rep, 11, 22291, https://doi.org/10.1038/s41598-021-01721-5, 2021.

Lu, X., Jacob, D. J., Zhang, Y., Shen, L., Sulprizio, M. P., Maasakkers, J. D., Varon, D. J., Qu, Z., Chen, Z., Hmiel, B., Parker, R. J., Boesch, H., Wang, H., He, C., and Fan, S.: Observation-derived 2010-2019 trends in methane emissions and intensities from US oil and gas fields tied to activity metrics, Proceedings of the National Academy of Sciences, 120, e2217900120, https://doi.org/10.1073/pnas.2217900120, 2023.

Maasakkers, J. D., McDuffie, E. E., Sulprizio, M. P., Chen, C., Schultz, M., Brunelle, L., Thrush, R., Steller, J., Sherry, C., Jacob, D. J., Jeong, S., Irving, B., and Weitz, M.: A Gridded Inventory of Annual 2012–2018 U.S. Anthropogenic Methane Emissions, Environ. Sci. Technol., 57, 16276–16288, https://doi.org/10.1021/acs.est.3c05138, 2023.

Nesser, H., Jacob, D. J., Maasakkers, J. D., Lorente, A., Chen, Z., Lu, X., Shen, L., Qu, Z., Sulprizio, M. P., Winter, M., Ma, S., Bloom, A. A., Worden, J. R., Stavins, R. N., and Randles, C. A.: High-resolution US methane emissions inferred from an inversion of 2019 TROPOMI satellite data: contributions from individual states, urban areas, and landfills, Atmospheric Chemistry and Physics, 24, 5069–5091, https://doi.org/10.5194/acp-24-5069-2024, 2024.

Omara, M., Himmelberger, A., MacKay, K., Williams, J. P., Benmergui, J., Sargent, M., Wofsy, S. C., and Gautam, R.: Constructing a measurement-based spatially explicit inventory of US oil and gas methane emissions, https://doi.org/10.5194/essd-2024-72, 2 April 2024.

Peischl, J., Eilerman, S. J., Neuman, J. A., Aikin, K. C., de Gouw, J., Gilman, J. B., Herndon, S. C., Nadkarni, R., Trainer, M., Warneke, C., and Ryerson, T. B.: Quantifying Methane and Ethane Emissions to the Atmosphere From Central and Western U.S. Oil and Natural Gas Production Regions, Journal of Geophysical Research: Atmospheres, 123, 7725–7740, https://doi.org/10.1029/2018JD028622, 2018.

Rienecker, M. M., Suarez, M. J., Todling, R., Bacmeister, J., Takacs, L., Liu, H.-C., Gu, W., Sienkiewicz, M., Koster, R. D., Gelaro, R., Stajner, I., and Nielsen, J. E.: The GEOS-5 Data Assimilation System-Documentation of Versions 5.0.1, 5.1.0, and 5.2.0, 2008.

Schwietzke, S., Pétron, G., Conley, S., Pickering, C., Mielke-Maday, I., Dlugokencky, E. J., Tans, P. P., Vaughn, T., Bell, C., Zimmerle, D., Wolter, S., King, C. W., White, A. B., Coleman, T., Bianco, L., and Schnell, R. C.: Improved Mechanistic Understanding of Natural Gas Methane Emissions from Spatially Resolved Aircraft Measurements, Environ. Sci. Technol., 51, 7286–7294, https://doi.org/10.1021/acs.est.7b01810, 2017.

Shen, L., Gautam, R., Omara, M., Zavala-Araiza, D., Maasakkers, J. D., Scarpelli, T. R., Lorente, A., Lyon, D., Sheng, J., Varon, D. J., Nesser, H., Qu, Z., Lu, X., Sulprizio, M. P., Hamburg, S. P., and Jacob, D. J.: Satellite quantification of oil and natural gas methane emissions in the US and Canada including contributions from individual basins, Atmospheric Chemistry and Physics, 22, 11203–11215, https://doi.org/10.5194/acp-22-11203-2022, 2022.

Sherwin, E., Rutherford, J., Zhang, Z., Chen, Y., Wetherley, E., Yakovlev, P., Berman, E., Jones, B., Thorpe, A., Ayasse, A., Duren, R., Brandt, A., and Cusworth, D.: Quantifying oil and natural gas system emissions using one million aerial site measurements, In Review, https://doi.org/10.21203/rs.3.rs-2406848/v1, 2023.

Varon, D. J., Jacob, D. J., Hmiel, B., Gautam, R., Lyon, D. R., Omara, M., Sulprizio, M., Shen, L., Pendergrass, D., Nesser, H., Qu, Z., Barkley, Z. R., Miles, N. L., Richardson, S. J., Davis, K. J., Pandey, S., Lu, X., Lorente, A., Borsdorff, T., Maasakkers, J. D., and Aben, I.: Continuous weekly monitoring of methane emissions from the

Permian Basin by inversion of TROPOMI satellite observations, Atmospheric Chemistry and Physics, 23, 7503–7520, https://doi.org/10.5194/acp-23-7503-2023, 2023.

Veefkind, J. P., Serrano-Calvo, R., de Gouw, J., Dix, B., Schneising, O., Buchwitz, M., Barré, J., van der A, R. J., Liu, M., and Levelt, P. F.: Widespread Frequent Methane Emissions From the Oil and Gas Industry in the Permian Basin, Journal of Geophysical Research: Atmospheres, 128, e2022JD037479, https://doi.org/10.1029/2022JD037479, 2023.

Warren, J. D., Sargent, M., Williams, J. P., Omara, M., Miller, C. C., Roche, S., MacKay, K., Manninen, E., Chulakadabba, A., Himmelberger, A., Benmergui, J., Zhang, Z., Guanter, L., Wofsy, S., and Gautam, R.: Sectoral contributions of high-emitting methane point sources from major US onshore oil and gas producing basins using airborne measurements from MethaneAIR, Atmospheric Chemistry and Physics, 25, 10661–10675, https://doi.org/10.5194/acp-25-10661-2025, 2025.

Zhang, Y., Gautam, R., Pandey, S., Omara, M., Maasakkers, J. D., Sadavarte, P., Lyon, D., Nesser, H., Sulprizio, M. P., Varon, D. J., Zhang, R., Houweling, S., Zavala-Araiza, D., Alvarez, R. A., Lorente, A., Hamburg, S. P., Aben, I., and Jacob, D. J.: Quantifying methane emissions from the largest oil-producing basin in the United States from space, Science Advances, 6, eaaz5120, https://doi.org/10.1126/sciadv.aaz5120, 2020.